



**HAL**  
open science

## Patterning Gold Nanorod Assemblies by Deep-UV Lithography

Céline Jégat, Edouard Rollin, Ludovic Douillard, Olivier Soppera, Keitaro Nakatani, Guillaume Laurent

► **To cite this version:**

Céline Jégat, Edouard Rollin, Ludovic Douillard, Olivier Soppera, Keitaro Nakatani, et al.. Patterning Gold Nanorod Assemblies by Deep-UV Lithography. *Journal of Physical Chemistry C*, 2022, 126 (32), pp.13729-13738. 10.1021/acs.jpcc.2c03047 . hal-03844169

**HAL Id: hal-03844169**

**<https://hal.science/hal-03844169v1>**

Submitted on 8 Nov 2022

**HAL** is a multi-disciplinary open access archive for the deposit and dissemination of scientific research documents, whether they are published or not. The documents may come from teaching and research institutions in France or abroad, or from public or private research centers.

L'archive ouverte pluridisciplinaire **HAL**, est destinée au dépôt et à la diffusion de documents scientifiques de niveau recherche, publiés ou non, émanant des établissements d'enseignement et de recherche français ou étrangers, des laboratoires publics ou privés.

# Patterning gold nanorod assemblies by deep-UV lithography

Céline Jégat,<sup>†</sup> Edouard Rollin,<sup>‡</sup> Ludovic Douillard,<sup>‡</sup> Olivier Soppera,<sup>§</sup> Keitaro Nakatani,<sup>†</sup> Guillaume Laurent<sup>†\*</sup>

<sup>†</sup> Université Paris-Saclay, ENS Paris-Saclay, CNRS UMR 8531, PPSM, 91190 Gif-sur-Yvette, France

<sup>‡</sup> Université Paris-Saclay, CEA SPEC, CNRS UMR 3680, 91190 Gif-sur-Yvette, France

<sup>§</sup> 1. Université de Haute Alsace, CNRS, IS2M UMR 7361, 68100, Mulhouse, France

2. Université de Strasbourg, Strasbourg, France

*Gold nanorod assembly, interferometric lithography, photoemission electron microscopy, near-field coupling*

---

**ABSTRACT:** We present a new method to pattern assemblies of gold nanorods (GNRs) on substrates and a study of the near-field coupling induced by the aggregation of the nanoparticles. Combination of deep-UV lithography and controlled deposition of functionalized GNRs generates complex GNR assemblies. Near-field coupling is investigated by photoemission electron microscopy (PEEM) on single, dimer and elongated aggregates of GNRs. This comparative study exhibits different kinds of near-field coupling efficiency that occur depending of the incident light polarization, inter-particle gaps and angles between the nanorods. Hot spots of the near field are associated to the inter-particle gap regions.

---

## INTRODUCTION

Metallic nanoparticles perform in many fields: photovoltaic,<sup>1</sup> modulation of molecular properties,<sup>2-5</sup> multimodal imaging,<sup>6</sup> photothermal therapy<sup>7,8</sup> and biosensing.<sup>9</sup> Indeed, light-matter interaction at the nanometric scale generates specific optical and electric properties, which can be driven by light. Localized surface plasmon resonances (LSPRs)<sup>10-12</sup> – coherent delocalized electron oscillations at the interface between a metal and a dielectric under a light stimulation – are the cornerstone of them.

Such properties are nowadays accessible at the nanometer scale by using techniques not limited by diffraction such as electron microscopy in electron energy loss mode EELS,<sup>13,14</sup> cathodoluminescence microscopy,<sup>15,16</sup> photo-induced near-field electron microscopy PINEM<sup>17,18</sup> or photoemission electron microscopy PEEM.<sup>19-22</sup> Among them, PEEM relies on a “photon in / electron out” interaction scheme based on an increase of the photoemission yield in the electromagnetic near field of the resonant nanoparticle. The higher the near field, the higher the photoemission yield. PEEM demonstrated solid capabilities in the near field investigation of single particles of various geometries<sup>23</sup> such as nanorods,<sup>24</sup> cubes,<sup>25</sup> triangles<sup>26</sup> or stars.<sup>27</sup> Since nanoparticle assemblies are promising materials, scientists actively pursued their investigations. In the following, PEEM is used to carry out a special multi-scale study of controlled nanoparticle assemblies from the single object up to large aggregates.

A better control of the assembly processes is important to optimize the near-field couplings. Several methods have been developed over the years to improve patterning such as surface functionalization,<sup>28,29</sup> funneled traps prepared by lithography,<sup>30</sup> solvent assisted self-assembly<sup>31,32</sup> or smectic oily streaks.<sup>33</sup> All of these methods try to strike a balance between inter-particle distance control (nanoscale) and large

2D area patterning (microscale), both mandatory for future meta-material applications.

In this work, we focus on a nanoparticle of basic geometry, namely a gold nanorod (GNR).<sup>34</sup> We developed a new method combining deep-UV lithography and suitable deposition conditions of GNRs with adapted functionalization to get GNR assemblies of controlled geometries. We used PEEM on such deposits to characterize the photoemission of (i) single GNR, (ii) GNR dimers and (iii) large elongated GNR aggregates. We finally performed theoretical calculations for a better understanding of the experimental results. In short, we proposed a new method for the development of controlled gold nanorod assemblies and characterized their near-field optics.

## EXPERIMENTAL METHODS

**Gold nanorod synthesis.** Gold nanorods<sup>35,36</sup> were synthesized according to Murray’s synthesis,<sup>37</sup> by mixing a seed solution and a growth solution and using a binary surfactant mixture<sup>38</sup> to get a better control of the aspect ratio. (i) Seed solution: 5 mL of HAuCl<sub>4</sub> solution (0,5 mM) were stirred at 50°C with 5 mL of cetyltrimethylammonium bromide (CTAB) solution (0,2 M). 1 mL of NaBH<sub>4</sub> (0,01 M) was added under vigorous stirring. The solution got brown because of the fast gold reduction. (ii) Growth solution: 3,5 g of CTAB, 0,617 g of sodium oleate (NaOL) and 125 mL of deionized water were mixed under stirring at 50°C. We added 29,15 mL of AgNO<sub>3</sub> (4 mM) to catalyze; waited for 15 minutes; and added 125 mL of HAuCl<sub>4</sub> (1 mM). While waiting for 90 minutes, the yellow growth solution got transparent because of the slow gold reduction. Finally, 2 mL of HCl (37 wt.%) were added before a 15 minutes wait. In a final gold reduction, we added 0,625 mL of ascorbic acid (0,064 M) under vigorous stirring. (iii) Mixture: 0,2 mL of the seed solution was vigorously stirred

with the growth solution. We waited for 14 h at room temperature to obtain the final GNRs ( $7,2 \cdot 10^{10}$  GNR / mL). Chemical products were purchased at Sigma-Aldrich and used them without any further purification. We synthesized two batches of GNRs. In synthesis 1 (previously described), the GNRs are  $81,2 \pm 0,1$  nm in length and  $20,0 \pm 0,1$  nm in width, meaning an aspect ratio of 4,06. In synthesis 2, the GNRs make  $115,6 \pm 0,1$  nm length and  $57,4 \pm 0,1$  nm broad, meaning an aspect ratio of 2,01. Figure 1 presents the extinction spectra (Cary 5000 UV-vis-NIR, Varian) and SEM images (Zeiss supra 40 MEB FEB, Gemini column) of these synthesis.

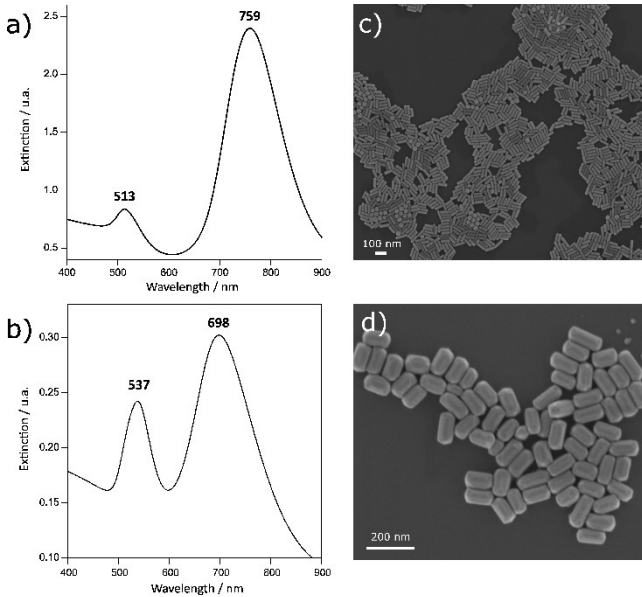


**Figure 1.** Extinction spectra of the gold nanorods used for (a) PEEM experiments (synthesis 1) and (b) deep-UV lithography (synthesis 2). (c-d) Corresponding SEM images.

**Gold nanorod functionalization.** To drive their organization on silicon wafer, GNRs were functionalized by sodium polystyrene sulfonate (PSS,  $M = 70\,000$  g/mol).<sup>39</sup> After removing the CTAB surrounding the gold nanorods (6000 rpm, relative centrifugal force  $RCF = 3\,461$  g, 20 minutes twice), we mixed 6 mL of the cleaned gold nanoparticle solution and 1,34 mL of a PSS solution (10 mg/mL) during 45 minutes at room temperature. A last centrifugation (12 000 rpm,  $RCF = 15\,455$  g, 10 minutes) allowed to remove the PSS excess remaining in the solution. The functionalized gold nanorods (GNRs@PSS) were redispersed in 6 mL of water.

**Gold nanorod depositions.** Preparation of self-assembled monolayers (SAMs) was conducted following a classical procedure, described in previous studies.<sup>40</sup> Substrates were silicon wafers, first cleaned by a 30 minutes UV-ozone irradiation (Bioforce Procleaner plus) and then immersed in silane precursor solution overnight. More precisely, the hexadecyltrichlorosilane (HTS, 95%, ABCR GbmH, 1 mM) solution was prepared in chloroform/cyclohexane (50/50 vol. %). HTS was used as received. After the reactions, the substrates were carefully rinsed to eliminate any remaining ungrafted precursors.

Photo-patterning of SAMs was conducted via deep-UV irradiation using an excimer laser emitting at 193 nm (Excistar from Coherent Inc.) and achieved using binary masks con-

sisting of metal lines on fused silica substrates. Hydrophilic functionalized strips' width is 850 nm while remaining hydrophobic areas' one is 750 nm (Figure S1.a).

GNRs@PSS (synthesis 2) were deposited on these functionalized surfaces by using one of the two following methods. (i) Droplet method. We put the surface on a 50°C hot plate, dropped 40  $\mu$ L of the GNRs@PSS solution on the surface and waited for the total evaporation of the solvent. (ii) Spin coating method. We put the surface on the spin coater headland, dropped 40  $\mu$ L of the GNRs@PSS solution on the surface and waited three minutes for a better spreading. Then, the surface was spun at 800 rpm (acceleration = 9) during 60 s and the solution leftover was evaporated by putting the surface on a 50°C hot plate.

**Photoemission electron microscopy measurements.** Photoemission electron microscopy measurements was performed on a previously described setup.<sup>22</sup> In short, the excitation of any LSPR strongly enhances the photoemission process. The obtained multiphoton photoemission electron maps thus reflect the actual distribution of the optical near field at the GNRs' surface.<sup>41,42</sup>

The GNRs were excited with the pulsed output of a Ti:Al<sub>2</sub>O<sub>3</sub> oscillator (Chameleon Ultra II, Coherent Inc., repetition rate 80 MHz, pulse width 150 fs) delivering photons in the  $\lambda = 690 - 1000$  nm wavelength range (1,80 – 1,24 eV). Peak power densities at the sample surface are in the range 0,5 – 5 GW/cm<sup>2</sup>. We can adjust the polarization of the laser beam from p- to s-polarization with a half-wave plate. Illumination is conducted at grazing incidence (angle  $\alpha = 72,5^\circ$  between light k-vector and sample surface normal) (Figure 2.a). We maintained constant fundamental parameters of the illuminating beam during the experiment – intensity, pulse time width and focus position – to acquire point by point wavelength (steps of 5 nm) and polarization dependence (steps of 5°) curves. We processed PEEM images with background correction and signal integration over regions of interest to determine the photoemission intensities.

The photoemission microscope (PEEM/LEEM III, Elmitec GmbH) operates under ultrahigh vacuum conditions. The setup can also record an image reflecting the topography of the sample by operating in low-energy electron imaging mode (LEEM) using the backscattered electrons. It achieves a spatial resolution down to 20 nm in PEEM imaging mode and close to 10 nm in LEEM mode. The topography images can be spatially correlated to the PEEM signatures.

To facilitate LEEM / PEEM experiments, additional simple GNR deposits (synthesis 1) have been carried out on conductive indium tin oxide (ITO)-coated glass substrate. Figures 2.b and 2.c display representative PEEM and LEEM signatures of individual GNRs on ITO glass substrate. As detailed below, no organization of the deposit is sought with these samples; the objective is to randomly disperse GNRs to access and characterize elementary building blocks of patterned GNR assemblies.

**Electromagnetic calculations.** Electromagnetic calculations were performed in order to confront theoretical results to the experimental ones. We used the MNPBEM Matlab toolbox<sup>43</sup> for the simulation of metallic nanoparticles. MNPBEM is based on a boundary element method (BEM) approach.

This

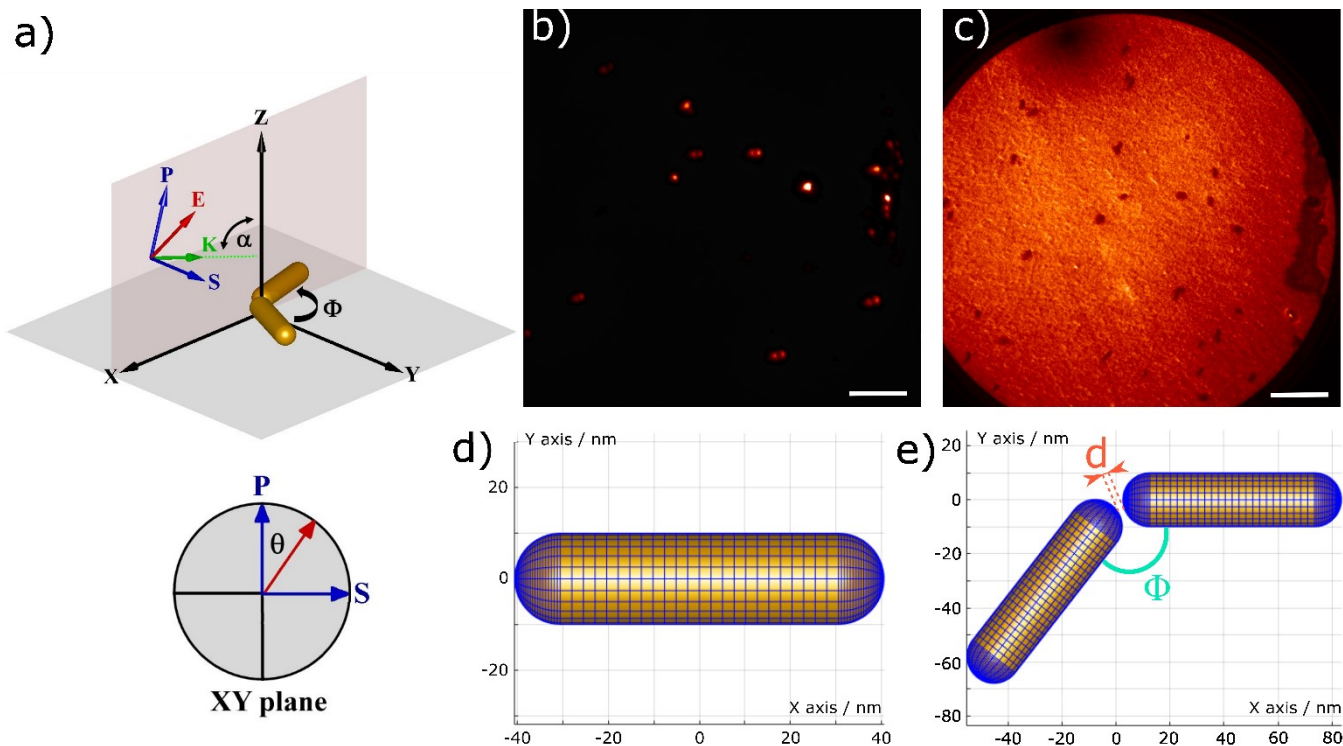


**Figure 2.** (a) Parameters of the system: grazing incidence angle  $\alpha$ , in-plane polarization angle  $\theta$ , dimer bisector angle  $\Phi$ , green arrow incident light wavevector, blue and red arrows light electric field. (b) PEEM imaging (excitation wavelength 710 nm) of dipolar LSPR signature of the GNRs, (c) LEEM imaging of individual GNRs. Scale bars for (b-c) codes for 500 nm. (d) Single gold nanorod model, using a MNPBEM trirod method to construct the discretized particle boundaries and (e) gold nanorod dimer model, with surface elements, dimer bisector angle  $\Phi$ , inter-particle gap distance  $d$ .

toolbox allows to design objects – separated by abrupt interfaces – of homogeneous dielectric functions. For interpretation purposes, two elementary geometrical configurations are considered: (i) an individual GNR 81 nm in length vs 20 nm in diameter (Figure 2.d) and (ii) a dimer of non-aligned GNRs with same previously mentioned dimensions (Figure 2.e). To discretize the particle boundaries, we used the MNPBEM trirod method with discretization parameter  $n = 25$ . Gold dielectric function is taken from Johnson and Christy<sup>44</sup> and the surrounding media is considered homogeneous with a refractive index set to 1.4. This value stands for an effective average of the substrate (indium thin oxide ITO, resp. Si) and the surrounding media contributions (vacuum). The incident angle of the excitation light beam is  $72.5^\circ$  (grazing incidence). Experimentally<sup>45</sup> for GNRs, the PEEM electron yield corresponds to a non-linear photoemission process (absorption) of order 6 in field magnitude. In BEM simulation, the photoemission response is computed from the field component normal to the object surface  $|E_{\perp}|$ . For each surface element, we first computed the scalar product between the surface normal vector and the total electromagnetic field, raised its magnitude to the power of 6 and summed up all the surface contributions. For individual object, we computed field distribution map and in-plane rotation dependence. For the GNR dimer, we additionally studied the impact of the gap distance  $d$  and the inter-particles angle between the two dimer units. In parallel to field maps, absorption and scattering spectra are computed. Descriptions in terms of integrated field and cross sections are equivalent. Light response of large elongated aggregates is qualitatively interpreted on the basis of the dimer model response.

## RESULTS AND DISCUSSION

**Gold nanorods deposition.** The aim of our approach is to generate aggregates with a controlled morphology (length and width) of a GNR single monolayer. First tries of CTAB-free GNRs showed no selectivity during the deposition process between the hydrophobic and hydrophilic strips. However, using GNRs@PSS led to a selective deposition of the nanoparticles in the hydrophilic strips as PSS drives the adsorption (Figures S1.b and S2).

We investigated several parameters with the droplet method (previously described in the experimental methods section) to get GNR organizations: surface irradiation dose, droplet volume and concentration of the GNRs@PSS solution (Figures S3-5). First, the higher the irradiation dose, the better the selectivity. This conforms with the deep-UV irradiation process: since the originally hydrophobic stripes turn during irradiation into hydrophilic ones by a photo-oxidative process,<sup>40</sup> the higher the dose, the higher the chemical contrast between irradiated and non-irradiated areas. Then, the higher the droplet volume, the higher the GNR density. However, no clear trend appears for the GNRs@PSS solution concentration: a low concentration does not generate elongated packings we seek and a high concentration entails multi-layered ones and a spatial selectivity decrease. A balance needs to be found depending of the concentration of the GNR solution.

With droplet method optimized parameters, we obtained GNR organizations on silicon wafer (Figure 3). Assemblies

occur near the droplet evaporation front and differ according to

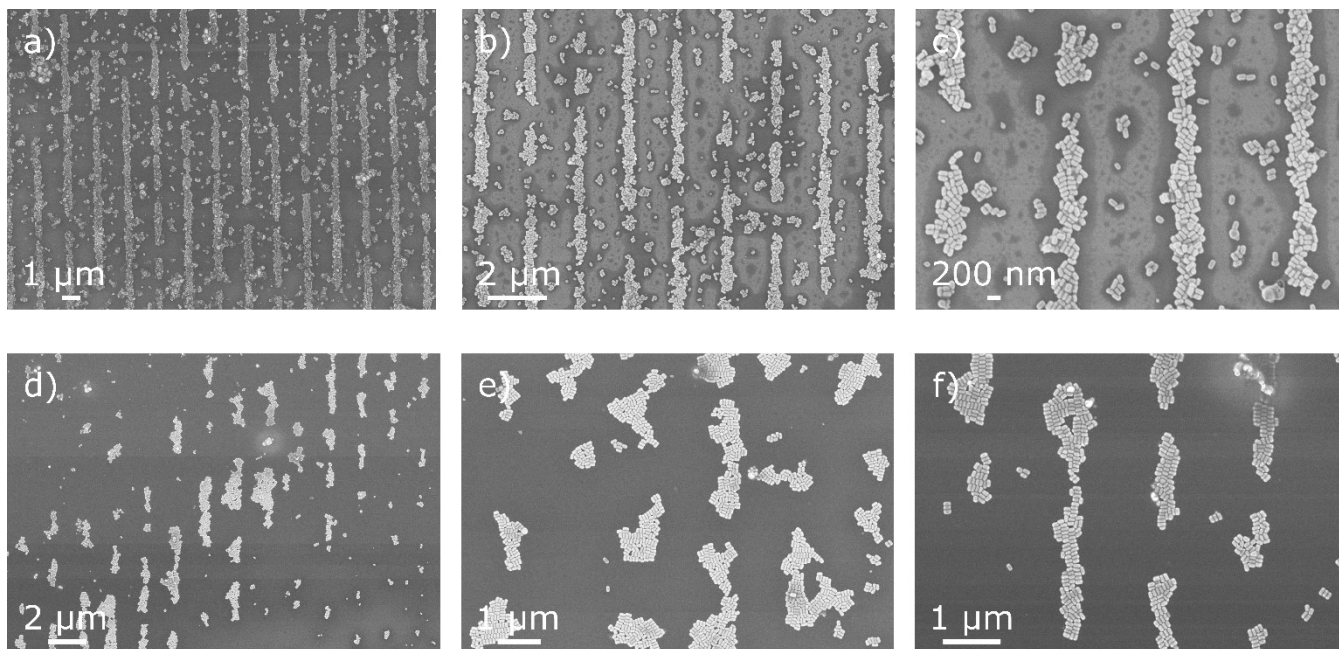


**Figure 4.** SEM images of gold nanorod deposits obtained by using (a-c) the droplet method (evaporation of a 40  $\mu\text{L}$  GNRs@PSS solution droplet on a 50°C hot silicon wafer) or (d-f) the spin coating method (after a 40  $\mu\text{L}$  GNRs@PSS solution droplet deposition on a silicon wafer and a 3 minute delay, ejection of the droplet at 800 rpm (acceleration = 9) during 60 s and evaporation of the residual on a 50°C hot plate)

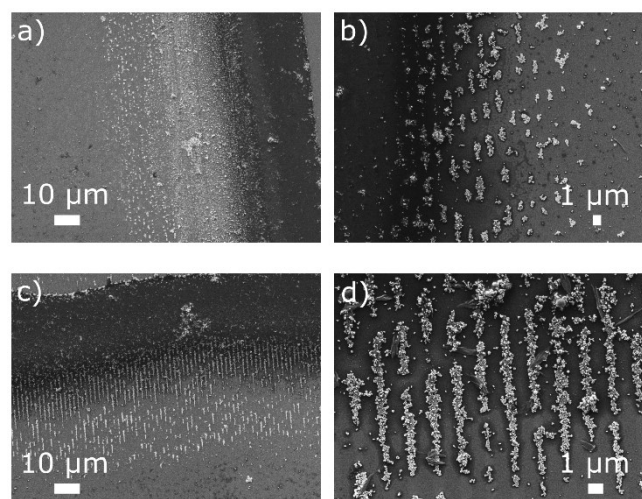


**Figure 3.** SEM images of a gold nanorod deposit. (a-b) Areas where the droplet front is parallel to the hydrophilic lines. GNR assemblies are 2  $\mu\text{m}$  long in average. (c-d) Areas where the droplet front is perpendicular to the hydrophilic lines. GNR assemblies are 6  $\mu\text{m}$  long in average.

the relative orientation of the evaporation front to the hydrophilic bands. Indeed, small GNR aggregates (average length of 2  $\mu\text{m}$ ) form when the droplet evaporation front is parallel to the hydrophilic strips (Figure 3.a-b) whereas larger elongated ones (average length of 6  $\mu\text{m}$ ) take shape when evaporation front and strips are perpendicular (Figure 3.c-d).

The droplet method gives elongated GNR aggregates with some residual amount of GNRs on hydrophobic strips and GNR multi-layers in some part of the assemblies (Figure 4.a-c). Inhomogeneous evaporation of the solvent and great sensitivity to nanoscopic local defects on the surface may

explain this drawback. Therefore, we investigated a spin coating method to tackle these issues.

With spin coating method optimized parameters (previously described in the experimental methods part), we obtained different GNR organizations on silicon wafer (Figure 4.d-f). First, the GNR aggregates are more compact in shape, meaning shorter and broader. Average dimensions are 2,5  $\mu\text{m}$  in length and 0,6  $\mu\text{m}$  in width, to be compared to 6,0  $\mu\text{m}$  in length and 0,4  $\mu\text{m}$  in width for assemblies obtained with the droplet method. Then, almost no residual GNRs stand between the GNR assemblies and these lasts are mono-layered. Hence the spin coating method distinctly improves the GNR deposits by increasing both the deposition selectivity and their mono-layer nature.

Thanks to the combination of chemical patterning and functionalized GNRs, selective deposition is achieved. The droplet method yields an important GNR density on the surface but the spin coating one exhibits more promising results by solving deposition selectivity and mono-layer nature issues.

From a geometrical point of view, single and dimer GNR units are the building blocks of GNR aggregates. Similarly, the optical response of an elongated aggregate can be qualitatively understood on the basis of those of its elementary building bricks. Hence we focused in a first step on the near field characterization of the single and non-aligned dimer GNR objects by photoemission microscopy.

**Characterization of a single gold nanorod.** As a reminder, the higher the local electromagnetic field of the GNR, the higher the photoemission signal; thus mapping the photoemission yield means studying the local electromagnetic field of the object.

Figures 2.b, 5.a and S6 display the photoemission response of a single GNR (synthesis 1), with a near-field distribution characteristic of a dipolar plasmon resonance with hot spots



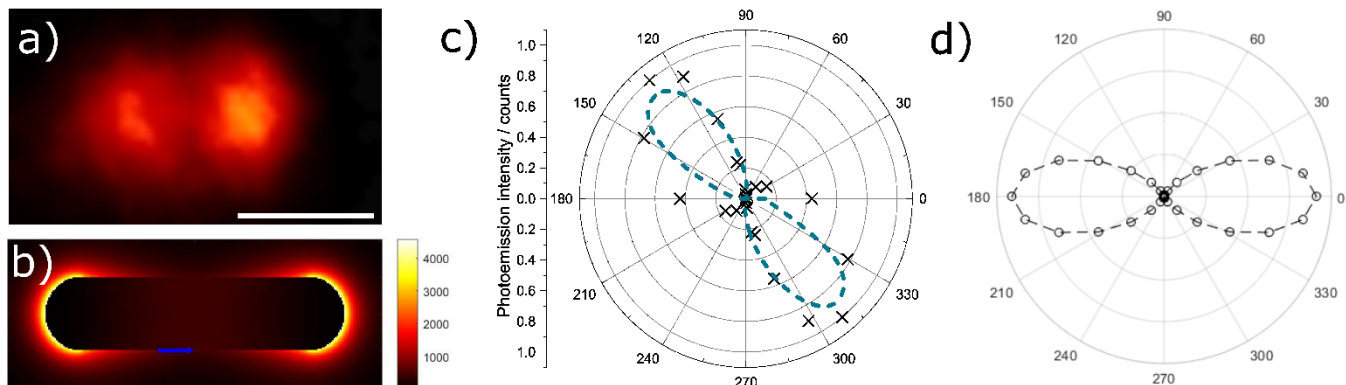


**Figure 5.** Nano-optics of a single GNR. Near field maps at dipolar plasmon resonance: (a) experimental PEEM imaging (excitation wavelength 710 nm) and (b) computed BEM  $|E|^2$  field map (excitation wavelength 731 nm). Reported blue arrow corresponds to in-plane electric field. Scale bar codes for 100 nm. Photoemission yield azimuthal dependences: (c) normalized integrated experimental PEEM signal (black crosses) and (d) normalized integrated computed BEM  $|E_{\perp}|^6$  field map. Light incidence angle  $72,5^{\circ}$ . The blue dashed lines are a fit of a  $\cos(\theta)^6$  function on the in-plane polarization angle  $\theta$ . Angular coordinate: in-plane polarization angle. Radial coordinate: normalized photoemission intensities.

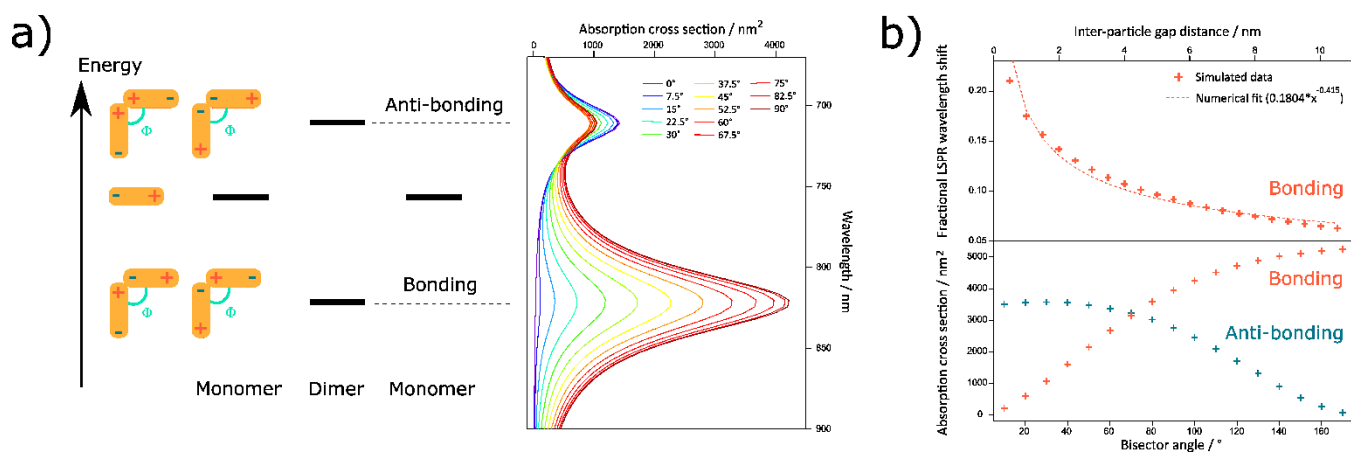


**Figure 6.** Nano-optics of a non-aligned GNR dimer – BEM simulation. (a) Plasmonic hybridization theory scheme. The bonding and anti-bonding energy levels are correlated with the calculated absorption cross section maxima, whose intensities change with the in-plane polarization angle  $\theta$  (bisector angle  $\Phi = 90^{\circ}$ ). (b) Fractional dependences of the dimer absorption cross section with the inter-particle gap distance  $d$  (bonding  $B_1$  eigenstate) and a change of the bisector angle (bonding  $B_1$  eigenstate  $\theta = 90^{\circ}$ , orange crosses, resp. anti-bonding  $A_1$  eigenstate  $\theta = 0^{\circ}$ , blue crosses).

of the electric field at both object ends. Associated LEEM imaging mode confirms the individual character of the object, meaning that no other colloidal objects are present within a distance of  $1 \mu\text{m}$  (Figure 2.c). Figure 5.c reports polarization dependence of the GNR photoemission signal under grazing incidence: we obtained a dipolar photoemission signature in accordance with previous works.<sup>46</sup> Moreover, the polarization dependence can be modelled by a  $\cos(\theta)^{2n}$  function, with  $n$  the number of needed absorbed photons for the photoemission of one electron to take place and  $\theta$  the in-plane azimuthal polarization angle.<sup>47</sup> Here, a  $\cos(\theta)^6$  simulation fits well the experimental data, pointing to a non-linear three photon absorption process. Computed field distribution map and in-plane rotation dependence support this result (Figures 5.b and 5.d).

**Characterization of a gold nanorod dimer.** A dimer of non-aligned GNRs exhibits a  $C_{2v}$  point group symmetry (substrate not considered). The latter possesses three symmetry operations in addition to identity. One of them, the principal rotation axis of order 2 ( $C_2(z)$ ) – aligned on the bisector angle

direction – defines the  $z$  axis according to the standard group theory (reference coordinate system of the dimer object). This principal axis constitutes the intersection of two perpendicular vertical mirror planes  $\sigma_{xz}$  and  $\sigma_{yz}$ . According to the  $C_{2v}$  character table,<sup>48</sup> the irreducible representation (irrep) of the dipolar resonance modes are of symmetry  $A_1(z)$ ,  $B_1(x)$  and  $B_2(y)$ . The 1D irrep  $A_1$  corresponds to a permanent electric dipole aligned on the principal axis  $z$ , the  $B_1$  one to a mode with its dipole aligned to axis  $x$  (within the dimer plane) and the  $B_2$  one to a mode with its dipole aligned to axis  $y$  (normal the dimer plane). According to the selection rules,<sup>25</sup> all three  $A_1$ ,  $B_1$  and  $B_2$  dipolar modes are optically active but only two of them are excited in a wavelength range close to the longitudinal resonance of the individual GNR (759 nm). These two states  $A_1$  and  $B_1$  correspond to excitations within the  $xz$  dimer plane (Figure S7.a). The  $B_2$  resonance is associated to the transverse resonance of an individual GNR.

Alternatively, these states can be described within the hybridization model,<sup>49</sup> here limited at low order to the cou-

pling

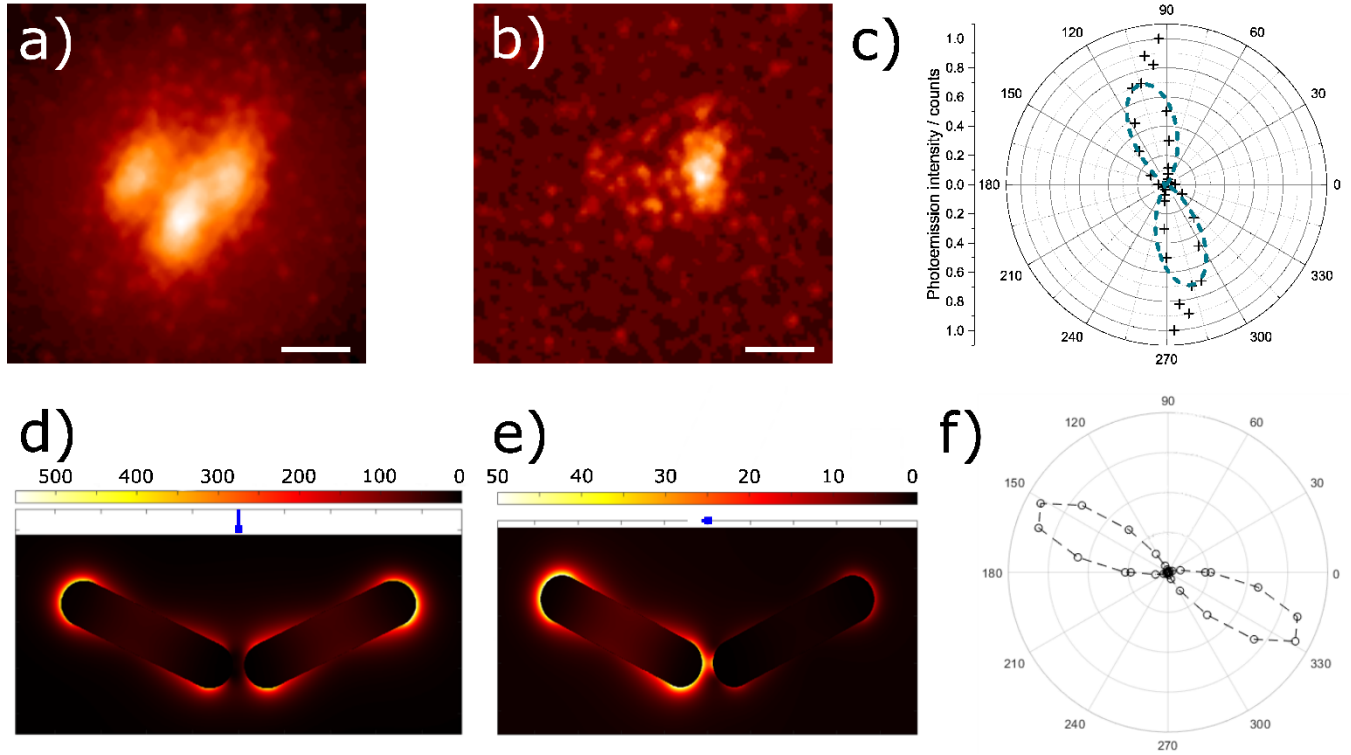


**Figure 7.** Nano-optics of a non-aligned GNR dimer. PEEM experiments: (a) near field map in anti-bonding eigenstate  $A_1$  (resonance wavelength), (b) near field map in bonding eigenstate  $B_1$  (off resonance) and (c) normalized azimuthal dependence. Excitation wavelength 730 nm. Scale bar codes for 20 nm. BEM computed results: computed BEM  $|E|^2$  field map (d) in anti-bonding eigenstate  $A_1$ , (e) in bonding eigenstate  $B_1$  and (f) normalized azimuthal dependence of integrated  $|E_z|^6$  field map. Excitation wavelength 704 nm ( $A_1$  eigenstate resonance). Reported blue arrow corresponds to in-plane electric field. Light incidence angle  $72.5^\circ$ . The blue dashed lines are a fit of a  $\cos(\theta)^6$  function on the in-plane polarization angle  $\theta$ . Angular coordinate: in-plane polarization angle. Radial coordinate: normalized photoemission intensities.

of the dipolar modes of two individual dimer components, meaning the coupling between high order modes is neglected. For a dimer, two hybridized states of respectively bonding ( $B_1$ ) and anti-bonding characters ( $A_1$ ) are expected. The anti-bonding resonance mode corresponds to a high-energy eigenvalue, while the bonding one is a bright mode of low energy eigenvalue.<sup>50</sup> Given the expected distributions of the electric charges, the anti-bonding eigenstate  $A_1$  generates a cold spot of the electric field in the gap region, whereas a hot spot is expected for the bonding eigenstate  $B_1$  (capacitive charge coupling in nature). Figure 6.a sums up the hybridization model for a non-aligned dimer model. The relative intensities of the different plasmon modes strongly depend on the inter-particle distance, the bisector angle and the interaction geometry of the GNR dimer in agreement with calculations based on the dipole-dipole interaction.<sup>50-52</sup>

In short, the absorption cross section of an individual prolate ellipsoid is well described by the Mie-Gans theory<sup>53</sup> and scales as the imaginary part of the object's polarizability  $\alpha$ , the ratio of the induced dipole to the exciting field  $\sigma_{\text{abs}} = k \cdot \text{Im}(\alpha)$ , with  $k$  the light wave vector. In a non-aligned dimer, the effective dipole of the bonding configuration scales geometrically with  $\sin(\Phi/2)$ , while the anti-bonding dipole scales with  $\cos(\Phi/2)$ , where  $\Phi$  is the bisector angle. Thus one ex-

pects similar qualitative behaviors for the GNR dimer absorption cross section (PEEM signature) with the bisector angle.

A GNR dimer is the smallest aggregate we can get. It also constitutes the basic building block of any GNR assemblies. To capture the fundamentals of the hybridization model, we performed numerical simulation in a BEM approach. Two degrees of freedom were more particularly investigated, namely the inter-particle gap distance in the contact region  $d$  and the dimer bisector angle  $\Phi$ . Two illumination geometries were considered: (i) either an anti-bonding eigenstate with an excitation field aligned along the dimer bisector direction ( $A_1$  symmetry state) or (ii) a bonding configuration where the excitation field is perpendicular to the bisector direction ( $B_1$  symmetry state).

Figure 6.b displays the action of a change of the inter-particle gap distance  $d$  on the fractional LSPR wavelength shift  $(\lambda - \lambda_0)/\lambda_0 = \Delta\lambda/\lambda_0$  in the bonding configuration ( $B_1$ ), with  $\lambda_0$  the longitudinal resonance wavelength of one individual GNR. The shorter the distance, the more intense the dipole coupling between both dimer components. Scaling of the fractional wavelength shift with inter-particle distance obeys a decreasing power law function of the form  $\Delta\lambda/\lambda_0 = A(d/D)^m$ , where  $A$  is a scaling constant and  $D$  the diameter of the



particle.<sup>52</sup> The computed absorption cross section follows an equivalent behaviour.<sup>54-56</sup>

Figure 6.b also describes the influence of a change of the bisector angle on the absorption cross section of the dimer in

the pure bonding ( $B_1$ ,  $\theta = 90^\circ$ ) and anti-bonding ( $A_1$ ,  $\theta = 0^\circ$ ) eigenstates. The absorption cross section of the anti-bonding

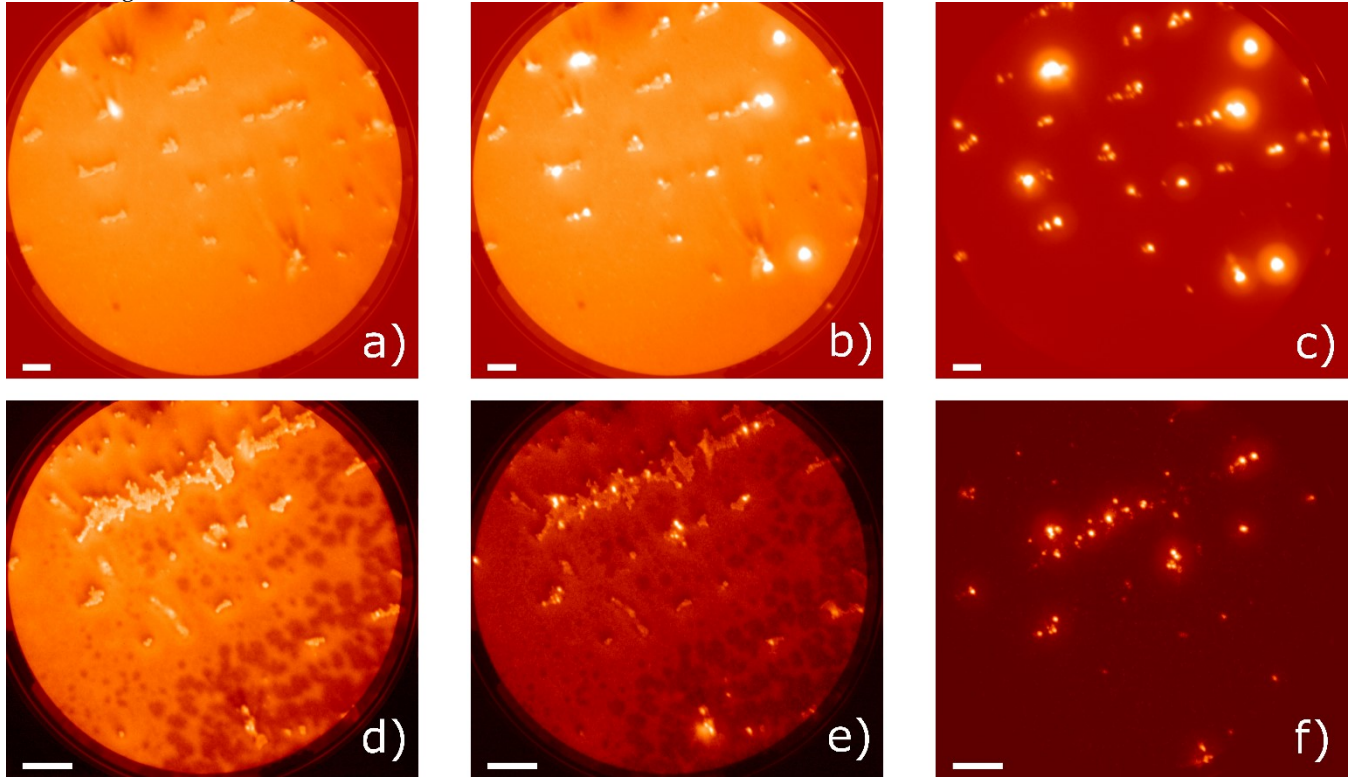


**Figure 8.** Study of elongated GNR assemblies on silicon wafer prepared by spin coating method. Small aggregates: images obtained in (a) LEEM imaging mode, (b) LEEM + PEEM imaging mode and (c) PEEM imaging mode (excitation wavelength 680 nm). Large aggregates: images obtained in (d) LEEM mode, (e) LEEM + PEEM mode and (f) PEEM mode. Scale bare codes for (a-c) 100 nm and (d-f) 400 nm. Light incidence angle  $72,5^\circ$ .

eigenstate scales roughly as  $\cos(\Phi/2)$  – respectively  $\sin(\Phi/2)$  for the bonding mode – as expected from simple geometrical considerations. The discrepancies are mainly due to the finite nature of the rod radii. Spectral positions of the hybridized states keep constant values whatever the bisector angle (Figure S8).<sup>51</sup> In more details, the resonance wavelength of the anti-bonding eigenstate  $A_1$  is 704 nm and  $B_1$  one is 884 nm.

Figure 7.d-e displays the maps of the near optical field for each of the configuration considered at 704 nm. Resonant excitation of the anti-bonding eigenvector  $A_1$  ( $\theta = 0^\circ$ ) yields to a significant near field response associated to the “cold spot” eigenstate. Correspondingly, off resonance excitation of the bonding eigenvector  $B_1$  ( $\theta = 90^\circ$ ) yields no significant signal.

These simulations provide the general framework for understanding the optical response of larger aggregates.

Experimentally, we isolated one representative dimer object (randomly chosen) and studied its photoemission response in PEEM mode. According to LEEM imaging (Figure S7.b), the bisector angle amounts to  $\Phi = 128^\circ \pm 2^\circ$  nm and the end-to-end distance in the particle gap region is close to  $d = 4 \text{ nm} \pm 1 \text{ nm}$ . Its field maps and in-plane azimuthal dependence of the photoemission signal (grazing incidence, fixed wavelength) are reported in Figures 7.a-c and S9. Photoemission signal azimuthal dependence is evaluated exper-

imentally by image integration of the photoemission electron yield as a function of the in-plane azimuthal direction of the exciting electric field. The experimental data are complemented by the corresponding results calculated by BEM (Figure 7.d-f). The PEEM angular photoemission signature follows a  $\cos(\theta)$ <sup>6</sup> behavior aligned on the bisector angle in agreement with the configuration in Figure 6.a. The non-linear order 6 of the azimuthal dependence originates from the non-linear nature of the photoelectric emission process (3 absorbed photons per photo-emitted electron), as in the case of the single GNR. Better contrast between eigenstates can be obtained close to their respective resonance wavelengths. The chosen wavelength of 710 nm is close to the resonance wavelength of the anti-bonding eigenstate  $A_1$  (704 nm). Hence, the brightest photoemission signal corresponds to excitation of the pure  $A_1$  eigenstate when the illuminating light excites an anti-bonding configuration of the rod pairs (Figure 7.d). Conversely, alignment of the excitation field with the bonding eigenstate direction yields a weak photoemission signal in response to a large spectral LSPR mismatch with the  $B_1$  resonance wavelength (Figure 7.e,  $B_1$  resonance wavelength 884 nm). In addition, please note that contrary to the numerical dimer model, experimentally both GNR dimer moieties are not alike. Some differences in length, width or crystallinity of the GNRs are to be expected.

### Characterization of elongated gold nanorod aggregates.

Large elongated GNR aggregates are complex assemblies, whose particle components distribute in sizes (length and diameter), relative orientations and positions. These distributions will result in numerous hybridized plasmon modes of distinct bonding characters. As demonstrated above in the case of a non-aligned dimer, the occurrence of a hot spot in the gap region implies the excitation of a plasmon eigenstate of bonding nature. Hence, in elongated GNR assemblies gap positions do not systematically generate hot spots under resonant excitation. Strong field enhancement at gap positions can only be achieved by locally exciting bonding plasmon eigenstates at the resonance wavelength.

In terms of optical behavior, elongated assemblies prepared by the spin coating method on silicon wafers exhibit numerous field hot spots under laser illumination (Figure 8). Average dimensions are 0,6  $\mu\text{m}$  in length for the small aggregates (example in Figure 8.a-c) and 2,5  $\mu\text{m}$  for the larger ones (example in Figure 8.d-f). The density of hot spots is high but remains well below the expected total number of contact regions in an elongated compact assembly of this size: roughly speaking, only 20% of topographically identifiable inter-particle gaps are hot spots under specific laser light illumination. Overall polarization dependences exhibit two distinct behaviors, either dipolar signatures reminiscent of those observed for a simple nonaligned GNR dimer or more complex – quadrupolar like – signatures (Figures S.10-11 for a detailed analysis). The  $\cos(\theta)^6$  dependence appear as a robust trend, in relation to the chemical nature of the golden objects. At the scale of the elongated assembly, one observes coupling between eigenstates of either bonding and anti-bonding characters. Local bonding configurations generate intense electric field hot spots, while cold spots are associated with locally anti-bonding configuration.

This description constitutes a crude view of the physics at play but helps to justify the presence of many hot spots at peculiar contact sites in the GNR aggregates. A more complete description would need to take into account more complex hybridization modes, their potential coupling (Fano resonance for example<sup>57,58</sup>) and cooperative effects. This description is beyond the scope of the present work.

### CONCLUSIONS

In this article, we developed a new method to organize nanoparticles on a surface, more precisely GNRs on silicon wafer. Indeed, we showed that the GNR functionalization by a polyelectrolyte significantly drives the adsorption of GNRs on the hydrophilic strips of the modified surface. We investigated two deposit methods, namely droplet evaporation and spin coating: each of them leads to partially ordered GNR assemblies. The second one maximizes the selectivity and the mono-layer nature of the aggregates. In future studies, GNR size and aspect ratio compared to the hydrophilic strip width will be taken into account. For example, reducing the width of the hydrophilic bands could result in narrower aggregates and thus better relative orientation of the GNRs (side-by-side and end-to-end) in the aggregate.

GNR ordering is the key point to develop efficient metamaterials for further applications, which will surely exhibit astounding properties. Near field electromagnetic behavior is a direct consequence of the aggregate ordering. To character-

ize the near field optics of GNR assemblies, we looked into the response of single GNRs, GNR dimers and GNR aggregates with photoemission electron microscopy (PEEM) and electromagnetic simulation (BEM). Investigation of elementary building blocks helps to justify the presence of electric field hot spots at peculiar contact sites in the aggregate.

Further control of the overall near field coupling in such complex GNR assemblies implies to pursue the development of the deposition methods.

### ASSOCIATED CONTENT

**Supporting Information.** Supplementary SEM images and theoretical calculation are in Supporting Information.

### AUTHOR INFORMATION

#### Corresponding Author

Guillaume Laurent: guillaume.laurent@ens-paris-saclay.fr

#### Author Contributions

All authors have given approval to the final version of the manuscript. GNR functionalization: CJ and GL. Deep-UV lithography: CJ and OS. LEEM/PEEM and BEM simulations: CJ and LD. Supervision: GL and KN.

### ACKNOWLEDGMENT

We thank Laurent Noël, Quentin Kirscher and Benjamin Leuschel (IS2M laboratory, Université de Haute-Alsace, France) for their precious help with the silica wafers functionalization. We also thank François Brisset (ICMMO laboratory, Université Paris-Saclay, France) and Ludovic Josien (IS2M laboratory, Université de Haute-Alsace, France) for the scanning electronic microscopy measurements. The authors acknowledge Fédération de recherche Chimie Physique Paris-Saclay (FR3510) for funding CJ's travel fees to IS2M.

### REFERENCES

- (1) Atwater, H. A.; Polman, A. Plasmonics for Improved Photovoltaic Devices. *Nat. Mater.* **2010**, *9* (3), 205–213. <https://doi.org/10.1038/nmat2629>.
- (2) Matsuda, K.; Yamaguchi, H.; Sakano, T.; Ikeda, M.; Tanifuji, N.; Irie, M. Conductance Photoswitching of Diarylethene-Gold Nanoparticle Network Induced by Photochromic Reaction. *J. Phys. Chem. C* **2008**, *112* (43), 17005–17010. <https://doi.org/10.1021/jp807479g>.
- (3) Van Der Molen, S. J.; Liao, J.; Kudernac, T.; Agustsson, J. S.; Bernard, L.; Calame, M.; Van Wees, B. J.; Feringa, B. L.; Schönenberger, C. Light-Controlled Conductance Switching of Ordered Metal-Molecule-Metal Devices. *Nano Lett.* **2009**, *9* (1), 76–80. <https://doi.org/10.1021/nl802487j>.
- (4) Ouhenia-Ouadahi, K.; Yasukuni, R.; Yu, P.; Laurent, G.; Pavageau, C.; Grand, J.; Guérin, J.; Léaustic, A.; Félidj, N.; Aubard, J.; Nakatani, K.;

- Métivier, R. Photochromic-Fluorescent-Plasmonic Nanomaterials: Towards Integrated Three-Component Photoactive Hybrid Nanosystems. *Chem. Commun.* **2014**, 50 (55), 7299–7302. <https://doi.org/10.1039/c4cc02179g>.
- (5) Noda, S.; Hasegawa, S.; Hamada, H.; Kobatake, S.; Imura, K. Plasmon Enhanced Optical Responses of Diarylethene Molecules Adsorbed on Gold Nanorods - Supp. *Chem. Lett.* **2019**, 48 (6), 537–540. <https://doi.org/10.1246/cl.190068>.
- (6) Reguera, J.; Jiménez De Aberasturi, D.; Henriksen-Lacey, M.; Langer, J.; Espinosa, A.; Szczupak, B.; Wilhelm, C.; Liz-Marzán, L. M. Janus Plasmonic-Magnetic Gold-Iron Oxide Nanoparticles as Contrast Agents for Multimodal Imaging. *Nanoscale* **2017**, 9 (27), 9467–9480. <https://doi.org/10.1039/c7nr01406f>.
- (7) Espinosa, A.; Bugnet, M.; Radtke, G.; Neveu, S.; Botton, G. A.; Wilhelm, C.; Abou-Hassan, A. Can Magneto-Plasmonic Nanohybrids Efficiently Combine Photothermia with Magnetic Hyperthermia? *Nanoscale* **2015**, 7 (45), 18872–18877. <https://doi.org/10.1039/c5nr06168g>.
- (8) Espinosa, A.; Curcio, A.; Cabana, S.; Radtke, G.; Bugnet, M.; Kolosnjaj-Tabi, J.; Péchoux, C.; Alvarez-Lorenzo, C.; Botton, G. A.; Silva, A. K. A.; Abou-Hassan, A.; Wilhelm, C. Intracellular Biodegradation of Ag Nanoparticles, Storage in Ferritin, and Protection by a Au Shell for Enhanced Photothermal Therapy. *ACS Nano* **2018**, 12 (7), 6523–6535. <https://doi.org/10.1021/acsnano.8b00482>.
- (9) Stuart, D. A.; Yuen, J. M.; Shah, N.; Lyandres, O.; Yonzon, C. R.; Glucksberg, M. R.; Walsh, J. T.; Van Duyne, R. P. In Vivo Glucose Measurement by Surface-Enhanced Raman Spectroscopy. *Anal. Chem.* **2006**, 78 (20), 7211–7215. <https://doi.org/10.1021/ac061238u>.
- (10) Barnes, W. L.; Dereux, A.; Ebbesen, T. W. Surface Plasmon Subwavelength Optics. *Nature* **2003**, 424 (6950), 824–830. <https://doi.org/10.1038/nature01937>.
- (11) Garcia, M. A. Surface Plasmons in Metallic Nanoparticles: Fundamentals and Applications. *J. Phys. D: Appl. Phys.* **2012**, 45, 283001. <https://doi.org/10.1088/0022-3727/45/38/389501>.
- (12) Amendola, V.; Pilot, R.; Frascioni, M.; Maragò, O. M.; Iati, M. A. Surface Plasmon Resonance in Gold Nanoparticles: A Review. *J. Phys. Condens. Matter* **2017**, 29 (20), 203001. <https://doi.org/10.1088/1361-648X/aa60f3>.
- (13) Nelayah, J.; Kociak, M.; Stéphan, O.; De Abajo, F. J. G.; Tencé, M.; Henrard, L.; Taverna, D.; Pastoriza-Santos, I.; Liz-Marzán, L. M.; Colliex, C. Mapping Surface Plasmons on a Single Metallic Nanoparticle. *Nat. Phys.* **2007**, 3 (5), 348–353. <https://doi.org/10.1038/nphys575>.
- (14) Rossouw, D.; Couillard, M.; Vickery, J.; Kumacheva, E.; Botton, G. A. Multipolar Plasmonic Resonances in Silver Nanowire Antennas Imaged with a Subnanometer Electron Probe. *Nano Lett.* **2011**, 11 (4), 1499–1504. <https://doi.org/10.1021/nl200634w>.
- (15) Knight, M. W.; Liu, L.; Wang, Y.; Brown, L.; Mukherjee, S.; King, N. S.; Everitt, H. O.; Nordlander, P.; Halas, N. J. Aluminum Plasmonic Nanoantennas. *Nano Lett.* **2012**, 12, 6000–6004. <https://doi.org/10.1021/nl303517v>.
- (16) Coenen, T.; Brenny, B. J. M.; Vesseur, E. J.; Polman, A. Cathodoluminescence Microscopy: Optical Imaging and Spectroscopy with Deep-Subwavelength Resolution. *MRS Bull.* **2015**, 40 (4), 359–365. <https://doi.org/10.1557/mrs.2015.64>.
- (17) Yurtsever, A.; Zewail, A. H. Direct Visualization of Near-Fields in Nanoplasmonics and Nanophotonics. *Nano Lett.* **2012**, 12 (6), 3334–3338. <https://doi.org/10.1021/nl301643k>.
- (18) Piazza, L.; Lummen, T. T. A.; Quiñonez, E.; Murooka, Y.; Reed, B. W.; Barwick, B.; Carbone, F. Simultaneous Observation of the Quantization and the Interference Pattern of a Plasmonic Near-Field. *Nat. Commun.* **2015**, 6, 8122. <https://doi.org/10.1038/ncomms7407>.
- (19) Cinchetti, M.; Gloskovskii, A.; Nepjiko, S. A.; Schönhense, G.; Rochholz, H.; Kreiter, M. Photoemission Electron Microscopy as a Tool for the Investigation of Optical near Fields. *Phys. Rev. Lett.* **2005**, 95 (4), 1–4. <https://doi.org/10.1103/PhysRevLett.95.047601>.
- (20) Chelaru, L. I.; Meyer zu Heringdorf, F. J. In Situ Monitoring of Surface Plasmons in Single-Crystalline Ag-Nanowires. *Surf. Sci.* **2007**, 601 (18), 4541–4545. <https://doi.org/10.1016/j.susc.2007.04.146>.
- (21) Aeschlimann, M.; Bauer, M.; Bayer, D.; Brixner, T.; García De Abajo, F. J.; Pfeiffer, W.; Rohmer, M.; Spindler, C.; Steeb, F. Adaptive Subwavelength Control of Nano-Optical Fields. *Nature* **2007**, 446 (7133), 301–304. <https://doi.org/10.1038/nature05595>.
- (22) Douillard, L.; Charra, F.; Fiorini, C.; Adam, P. M.; Bachelot, R.; Kostcheev, S.; Lerondel, G.; De La Chapelle, M. L.; Royer, P. Optical Properties of Metal Nanoparticles as Probed by Photoemission Electron Microscopy. *J. Appl.*

- Phys.* **2007**, *101* (8), 083518. <https://doi.org/10.1063/1.2719282>.
- (23) Daniel, M. C.; Astruc, D. Gold Nanoparticles: Assembly, Supramolecular Chemistry, Quantum-Size-Related Properties, and Applications Toward Biology, Catalysis, and Nanotechnology. *Chem. Rev.* **2004**, *104* (1), 293–346. <https://doi.org/10.1021/cr030698+>.
- (24) Ming, T.; Zhao, L.; Yang, Z.; Chen, H.; Sun, L.; Wang, J.; Yan, C. Strong Polarization Dependence of Plasmon-Enhanced Fluorescence on Single Gold Nanorods. *Nano Lett.* **2009**, *9* (11), 3896–3903. <https://doi.org/10.1021/nl902095q>.
- (25) Mitiche, S.; Marguet, S.; Charra, F.; Douillard, L. Near-Field Localization of Single Au Cubes: A Group Theory Description. *J. Phys. Chem. C* **2017**, *121* (8), 4517–4523. <https://doi.org/10.1021/acs.jpcc.6b10585>.
- (26) Awada, C.; Popescu, T.; Douillard, L.; Charra, F.; Perron, A.; Yockell-Lelièvre, H.; Baudrion, A. L.; Adam, P. M.; Bachelot, R. Selective Excitation of Plasmon Resonances of Single Au Triangles by Polarization-Dependent Light Excitation. *J. Phys. Chem. C* **2012**, *116* (27), 14591–14598. <https://doi.org/10.1021/jp303475c>.
- (27) Hrelescu, C.; Sau, T. K.; Rogach, A. L.; Jäckel, F.; Laurent, G.; Douillard, L.; Charra, F. Selective Excitation of Individual Plasmonic Hotspots at the Tips of Single Gold Nanostars. *Nano Lett.* **2011**, *11* (2), 402–407. <https://doi.org/10.1021/nl103007m>.
- (28) Nie, Z.; Fava, D.; Kumacheva, E.; Zou, S.; Walker, G. C.; Rubinstein, M. Self-Assembly of Metal-Polymer Analogues of Amphiphilic Triblock Copolymers. *Nat. Mater.* **2007**, *6* (8), 609–614. <https://doi.org/10.1038/nmat1954>.
- (29) Tan, S. J.; Campolongo, M. J.; Luo, D.; Cheng, W. Building Plasmonic Nanostructures with DNA. *Nat. Nanotechnol.* **2011**, *6* (5), 268–276. <https://doi.org/10.1038/nnano.2011.49>.
- (30) Flauraud, V.; Mastrangeli, M.; Bernasconi, G. D.; Butet, J.; Alexander, D. T. L.; Shahrabi, E.; Martin, O. J. F.; Brugger, J. Nanoscale Topographical Control of Capillary Assembly of Nanoparticles. *Nat. Nanotechnol.* **2017**, *12* (1), 73–80. <https://doi.org/10.1038/nnano.2016.179>.
- (31) Hanske, C.; Hill, E. H.; Vila-Liarte, D.; González-Rubio, G.; Matricardi, C.; Mihi, A.; Liz-Marzán, L. M. Solvent-Assisted Self-Assembly of Gold Nanorods into Hierarchically Organized Plasmonic Mesostuctures. *ACS Appl. Mater. Interfaces* **2019**, *11* (12), 11763–11771. <https://doi.org/10.1021/acsami.9b00334>.
- (32) Abtahi, S. M. H.; Burrows, N. D.; Idesis, F. A.; Murphy, C. J.; Saleh, N. B.; Vikesland, P. J. Sulfate-Mediated End-to-End Assembly of Gold Nanorods. *Langmuir* **2017**, *33* (6), 1486–1495. <https://doi.org/10.1021/acs.langmuir.6b04114>.
- (33) Do, S. P. hen.; Missaoui, A.; Coati, A.; Coursault, D.; Jeridi, H.; Resta, A.; Goubet, N.; Wojcik, M. M.; Choux, A.; Royer, S.; Briand, E.; Donnio, B.; Gallani, J. L.; Pansu, B.; Lhuillier, E.; Garreau, Y.; Babonneau, D.; Goldmann, M.; Constantin, D.; Gallas, B.; Croset, B.; Lacaze, E. From Chains to Monolayers: Nanoparticle Assembly Driven by Smectic Topological Defects. *Nano Lett.* **2020**, *20* (3), 1598–1606. <https://doi.org/10.1021/acs.nanolett.9b04347>.
- (34) Vigderman, L.; Khanal, B. P.; Zubarev, E. R. Functional Gold Nanorods: Synthesis, Self-Assembly, and Sensing Applications. *Adv. Mater.* **2012**, *24* (36), 4811–4841. <https://doi.org/10.1002/adma.201201690>.
- (35) Jana, N. R.; Gearheart, L.; Murphy, C. J. Wet Chemical Synthesis of High Aspect Ratio Cylindrical Gold Nanorods. *J. Phys. Chem. B* **2001**, *105* (19), 4065–4067. <https://doi.org/10.1021/jp0107964>.
- (36) Jana, N. R.; Gearheart, L.; Murphy, C. J. Seed-Mediated Growth Approach for Shape-Controlled Synthesis of Spheroidal and Rod-like Gold Nanoparticles Using a Surfactant Template. *Adv. Mater.* **2001**, *13* (18), 1389–1393. [https://doi.org/10.1002/1521-4095\(200109\)13:18<1389::AID-ADMA1389>3.o.CO;2-F](https://doi.org/10.1002/1521-4095(200109)13:18<1389::AID-ADMA1389>3.o.CO;2-F).
- (37) Ye, X.; Zheng, C.; Chen, J.; Gao, Y.; Murray, C. B. Using Binary Surfactant Mixtures to Simultaneously Improve the Dimensional Tunability and Monodispersity in the Seeded Growth of Gold Nanorods. *Nano Lett.* **2013**, *13* (2), 765–771. <https://doi.org/10.1021/nl304478h>.
- (38) Nikoobakht, B.; El-Sayed, M. A. Preparation and Growth Mechanism of Gold Nanorods (NRs) Using Seed-Mediated Growth Method. *Chem. Mater.* **2003**, *15* (10), 1957–1962. <https://doi.org/10.1021/cm020732l>.
- (39) Jégat, C.; Laurent, G. Layer-by-Layer Functionalization of Gold Nanorods by Polyelectrolytes to Control Surface Spacer and Precisely Tune the Surface Plasmon Resonance Position. *Chem. Lett.* **2021**, *50* (3), 426–430. <https://doi.org/10.1246/cl.200687>.
- (40) Leuschel, B.; Gwiazda, A.; Heni, W.; Diot, F.; Yu, S. Y.; Bidaud, C.; Vonna, L.; Ponche, A.; Haidara, H.; Soppera, O. Deep-UV Photoinduced Chemical Patterning at the Micro- and Nanoscale for Directed Self-

- Assembly. *Sci. Rep.* **2018**, *8* (1), 1–15. <https://doi.org/10.1038/s41598-018-28196-1>.
- (41) Schmidt, O.; Bauer, M.; Wiemann, C.; Porath, R.; Scharte, M.; Andreyev, O.; Schönhense, G.; Aeschlimann, M. Time-Resolved Two Photon Photoemission Electron Microscopy. *Appl. Phys. B Lasers Opt.* **2002**, *74* (3), 223–227. <https://doi.org/10.1007/s003400200803>.
- (42) Kubo, A.; Onda, K.; Petek, H.; Sun, Z.; Jung, Y. S.; Kim, H. K. Femtosecond Imaging of Surface Plasmon Dynamics in a Nanostructured Silver Film. *Nano Lett.* **2005**, *5* (6), 1123–1127. <https://doi.org/10.1021/nl0506655>.
- (43) Hohenester, U.; Trügler, A. MNPBEM - A Matlab Toolbox for the Simulation of Plasmonic Nanoparticles. *Comput. Phys. Commun.* **2012**, *183* (2), 370–381. <https://doi.org/10.1016/j.cpc.2011.09.009>.
- (44) P. B. Johnson and R. W. Christy. Optical Constant of the Noble Metals. *Phys. L Re View B* **1972**, *6* (12), 4370–4379.
- (45) Awada, C.; Barbillon, G.; Charra, F.; Douillard, L.; Greffet, J. J. Experimental Study of Hot Spots in Gold/Glass Nanocomposite Films by Photoemission Electron Microscopy. *Phys. Rev. B - Condens. Matter Mater. Phys.* **2012**, *85* (4). <https://doi.org/10.1103/PhysRevB.85.045438>.
- (46) Douillard, L.; Charra, F.; Korczak, Z.; Bachelot, R.; Kostcheev, S.; Lerondel, G.; Adam, P. M.; Royer, P. Short Range Plasmon Resonators Probed by Photoemission Electron Microscopy. *Nano Lett.* **2008**, *8* (3), 935–940. <https://doi.org/10.1021/nl080053v>.
- (47) Pramod, P.; Thomas, K. G. Plasmon Coupling in Dimers of Au Nanorods. *Adv. Mater.* **2008**, *20* (22), 4300–4305. <https://doi.org/10.1002/adma.200703057>.
- (48) C2v character table <http://symmetry.jacobs-university.de/cgi-bin/group.cgi?group=904&option=4>.
- (49) Nordlander, P.; Oubre, C.; Prodan, E.; Li, K.; Stockman, M. I. Plasmon Hybridization in Nanoparticle Dimers. *Nano Lett.* **2004**, *4* (5), 899–903. <https://doi.org/10.1021/nl049681c>.
- (50) Wu, J.; Lu, X.; Zhu, Q.; Zhao, J.; Shen, Q.; Zhan, L.; Ni, W. Angle-Resolved Plasmonic Properties of Single Gold Nanorod Dimers. *Nano-Micro Lett.* **2014**, *6* (4), 372–380. <https://doi.org/10.1007/s40820-014-0011-7>.
- (51) Shao, L.; Woo, K. C.; Chen, H.; Jin, Z.; Wang, J.; Lin, H. Q. Angle-and Energy-Resolved Plasmon Coupling in Gold Nanorod Dimers. *ACS Nano* **2010**, *4* (6), 3053–3062. <https://doi.org/10.1021/nn100180d>.
- (52) Funston, A. M.; Novo, C.; Davis, T. J.; Mulvaney, P. Plasmon Coupling of Gold Nanorods at Short Distances and in Different Geometries. *Nano Lett.* **2009**, *9* (4), 1651–1658.
- (53) Gans, R. Über Die From Ultramikroskopischer Goldteilchen. *Ann. Phys.* **1912**, *342*, 881–900.
- (54) Su, K. H.; Wei, Q. H.; Zhang, X.; Mock, J. J.; Smith, D. R.; Schultz, S. Interparticle Coupling Effects on Plasmon Resonances of Nanogold Particles. *Nano Lett.* **2003**, *3* (8), 1087–1090. <https://doi.org/10.1021/nl034197f>.
- (55) Jain, P. K.; Huang, W.; El-sayed, M. A. On the Universal Scaling Behavior of the Distance Decay of Plasmon Coupling in Metal Nanoparticle Pairs: A Plasmon Ruler Equation. *Nano Lett.* **2007**, *7* (7), 2080–2088.
- (56) Huang, C. P.; Yin, X. G.; Kong, L. B.; Zhu, Y. Y. Interactions of Nanorod Particles in the Strong Coupling Regime. *J. Phys. Chem. C* **2010**, *114* (49), 21123–21131. <https://doi.org/10.1021/jp1074362>.
- (57) Yang, Z. J.; Hao, Z. H.; Lin, H. Q.; Wang, Q. Q. Plasmonic Fano Resonances in Metallic Nanorod Complexes. *Nanoscale* **2014**, *6* (10), 4985–4997. <https://doi.org/10.1039/c3nr06502b>.
- (58) Lovera, A.; Gallinet, B.; Nordlander, P.; Martin, O. J. F. Mechanisms of Fano Resonances in Coupled Plasmonic Systems. *ACS Nano* **2013**, *7* (5), 4527–4536.

